RAPID COMMUNICATION

Tailoring electronic properties of two-dimensional antimonene with isoelectronic counterparts*

Ye Zhang(张也)[1], Huai-Hong Guo(郭怀红)[1,†], Bao-Juan Dong(董宝娟)[2,4,5,‡], Zhen Zhu(朱震)[3,§], Teng Yang(杨腾)[2,¶], Ji-Zhang Wang (王吉章)[2], and Zhi-Dong Zhang(张志东)[2]

[1] *College of Sciences, Liaoning Shihua University, Fushun* 113001, *China*
[2] *Shenyang National Laboratory for Materials Science, Institute of Metal Research, Chinese Academy of Sciences, Shenyang* 110016, *China*
[3] *Materials Department, University of California, Santa Barbara, CA* 93106, *USA*
[4] *State Key Laboratory of Quantum Optics and Quantum Optics Devices, Institute of Opto-Electronics, Shanxi University, Taiyuan* 030006, *China*
[5] *Collaborative Innovation Center of Extreme Optics, Shanxi University, Taiyuan* 030006, *China*

(Received 18 December 2019; revised manuscript received 6 January 2020; accepted manuscript online 16 January 2020)

Using *ab initio* density functional theory calculations, we explore the three most stable structural phases, namely, α, β, and cubic (c) phases, of two-dimensional (2D) antimonene, as well as its isoelectronic counterparts SnTe and InI. We find that the band gap increases monotonically from Sb to SnTe to InI along with an increase in ionicity, independent of the structural phases. The band gaps of this material family cover the entire visible-light energy spectrum, ranging from 0.26 eV to 3.37 eV, rendering them promising candidates for optoelectronic applications. Meanwhile, band-edge positions of these materials are explored and all three types of band alignments can be achieved through properly combining antimonene with its isoelectronic counterparts to form heterostructures. The richness in electronic properties for this isoelectronic material family sheds light on possibilities to tailor the fundamental band gap of antimonene via lateral alloying or forming vertical heterostructures.

Keywords: tailoring electronic properties, two-dimensional antimonene, isoelectronic counterparts

PACS: 73.61.Cw, 61.46.–w, 73.22.–f **DOI:** 10.1088/1674-1056/ab6c4e

1. Introduction

Since the discovery of graphene[1] in 2004, two-dimensional (2D) materials have attracted tremendous research efforts in both theory and experiment due to their fundamental novelty and technological importance. Applications of the 2D materials are found in a broad field, including field effect transistors, electrocatalysts, optoelectronics, spintronics, and so on, which in general require a tunable band gap, high carrier mobility, and excellent chemical stability. Along the journey of chasing for a "magic" material satisfying the aforementioned requirements, the 2D family has largely expanded and now includes graphene and its group-IV counterparts (silicene, germanene), transition metal dichalcogenides (TMDs),[2–6] transition metal monochalcogenides,[7–9] phosphorene[10–15] and its group-V counterparts antimonene and arsenene,[16–18] and many others.[19] In addition, the success in patterning heterostructures by using distinct 2D materials[20] has further enlarged the 2D family. Searching for systems with small lattice mismatch but different electronic properties is essential to achieve such heterostructures, which can not only enrich the 2D family, but also increase the tunability.

Recently, isoelectronic materials design has been proposed to search for systems with similarity in both structure and electronic structure.[21] It has been successfully applied to phosphorene, a promising 2D semiconductor with high mobility and high on/off ratio, leading to the discovery of 2D arsenene,[17] antimonene,[22] and SiS.[21] In this way, the structural and electronic properties of the phosphorene isoelectronic family have been largely enriched. Especially, monolayer antimonene,[22–24] a member of phosphorene isoelectronic family, has been successfully synthesized, which even shows superior electronic properties and chemical stability over phosphorene. We believe that, along with the naturally existing InI and SnTe – the isoelectronic counterpart of antimonene, it is very likely to tailor 2D antimonene with high tunability via isoelectronic alloying or heterostructure patterning with them. Therefore, it is critical to understand the subtlety between the isoelectronic systems for the controllable functionality design based on 2D antimonene.

*Project supported by the National Natural Science Foundation of China (Grant No. 51702146), the College Students' Innovation and Entrepreneurship Projects, China (Grant No. 201710148000072), and Liaoning Province Doctor Startup Fund, China (Grant No. 201601325).

†Corresponding author. E-mail: hhguo@escience.cn
‡Corresponding author. E-mail: dongbaojuan.1989@gmail.com
§Corresponding author. E-mail: zhuzhen@engineering.ucsb.edu
¶Corresponding author. E-mail: yangteng@imr.ac.cn

© 2020 Chinese Physical Society and IOP Publishing Ltd

Previous experimental and theoretical studies have shown that group-V elemental materials and their isoelectronic counterparts can crystallize in three typical structural phases, namely, α, β, and cubic (c) phases, as illustrated in Fig. 1. For example, the α-phase of the space group $Pmn2_1$ is energetically the most favorable for phosphorene,[25] the β-phase in the space group $P3m1$ is more preferable over other phases for both arsenene and antimonene,[22] and the most stable phase for monolayer InI[26] is the c-phase of $P4/nmm$. In the present work, we have thoroughly explored the structure and electronic structure of antimonene and its isoelectronic counterparts (SnTe and InI) in all the three phases, and the tunability of 2D antimonene by means of isoelectronic alloying or heterostructure patterning among them, using hybrid density functional calculations and screening genetic algorithm. The computational method is described in Section 2. Then, we discuss the relative structural stability of the three phases in Subsection 3.1, followed by our results and discussion on their electronic properties, as well as band alignments in Subsection 3.2 and band structures for vertical and alloying heterostructures in Subsection 3.3. Finally, we summarize our key findings in Section 4.

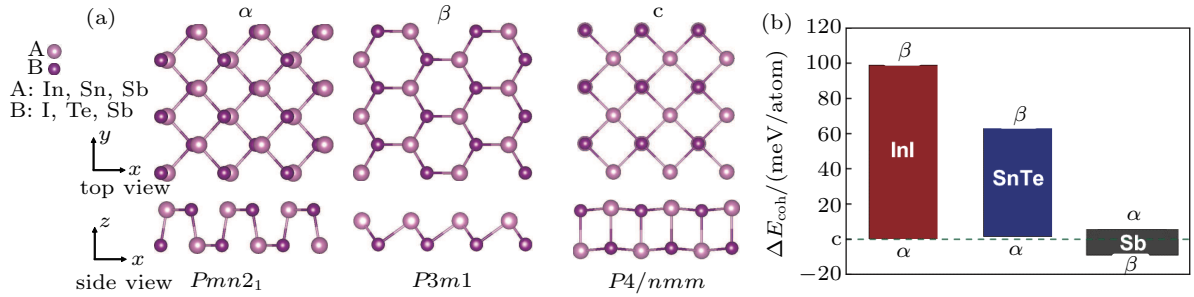

Fig. 1. Structure and stability. (a) Atomic structure of 2D antimonene and its isoelectronic counterparts in the three typical phases α, β, and c, with constituents A (B) in light (dark) purple representing In (I), Sn (Te), and Sb (Sb) atoms, respectively. The corresponding space group is given under each structure. (b) Cohesive energy difference $\Delta E_{\rm coh}$ between α, β phases and c phase, here the cohesive energy of the c phase as a reference is set to be zero, α and β lie either at the bottom or on top of the rectangle.

2. Computational methods

All of our calculations are performed within *ab initio* density functional theory as implemented in the Vienna *ab initio* simulation package (VASP).[27] We use a periodic boundary condition with monolayer structures represented by a periodic array of slabs separated by a vacuum region ($\geq$ 15 Å). The projector augmented wave (PAW) pseudopotentials[28] and the Perdew–Burke–Ernzerhof (PBE)[29] exchange–correlation functional within the general gradient approximation (GGA) are used. For evaluating the electronic properties and band alignments, hybrid-functional (HSE) is used, which is in general accurate in band gap and band alignment prediction for semiconducting systems.[30] The Brillouin zone of the primitive unit cell of the 2D structures is sampled in the Monkhorst–Pack integration scheme[31] by 13×13×1 k-points for the GGA calculation and 7×7×1 k-points for the HSE calculation. We adopt 500 eV as the electronic kinetic energy cutoff for the plane-wave basis and 10^{-6} eV for a total energy difference between subsequent self-consistency iterations as the criterion for reaching self-consistency. All geometries are optimized using the conjugate gradient method[32] until none of the residual Hellmann–Feynman forces exceeds 1×10^{-2} eV/Å. The optB88-type vdW corrections[33] usually gives a better agreement with the experiment than the other types of vdW correction, not only on the interlayer lattice size but also on the in-layer lattice parameters. Therefore, PBE with the optB88-vdW correction is used to relax the atomic structures.

The second-order harmonic interatomic force constants (IFCs) and phonon dispersion relations are calculated by the PHONOPY package[34] based on density functional perturbation theory.[35] A 3×3×1 supercell size and 7×7×1 q mesh are used to calculate the dynamical matrix in the whole Brillouin zone.

The optical absorption spectrum is calculated based on the real (ε') and imaginary (ε'') parts of the dielectric function as a function of laser energy. The imaginary part is determined by a summation over empty states using the equation[36]

$$\varepsilon''_{\alpha\beta}(\omega) = \frac{4\pi^2e^2}{\Omega}\lim_{q\to0}\sum_{c,v,k}2w_k\delta(\varepsilon_{ck}-\varepsilon_{vk}-\omega) \times\langle u_{ck+e_\alpha q}|u_{vk}\rangle\langle u_{ck+e_\beta q}|u_{vk}\rangle^*,$$

where c and v refer to the conduction and valence band states, respectively, and u_{ck} is the periodic part of the orbitals at k point. The real dielectric tensor ε' is obtained by the usual Kramers–Kronig transformation. The extinction coefficient[37] is $\kappa=\sqrt{(\sqrt{\varepsilon'^2+\varepsilon''^2}-\varepsilon')/2}$. The absorption coefficient α is given by $\alpha=4\pi\kappa E_{\rm L}/(hc)$, where $E_{\rm L}$ is the incident laser excitation energy, h is the Planck constant, and c is the speed of light in the vacuum.

3. Results and discussion

3.1. Structures and stabilities

For antimonene and its isoelectronic systems, we take three typical phases α, β, and cubic as the starting structures, which are shown in Fig. 1. α and β are the stable structural phases of black and blue phosphorene, which have symmetry groups of $Pmn2_1$ and $P3m1$, respectively. The c phase is the cubic phase in symmetry group $P4/nmm$, which was found to be stable in InI monolayer as reported in our recent work.[26] All the three structures of Sb and its isoelectronic materials are fully relaxed, with the optimized structures shown in Fig. A1 and structural parameters including lattice constants and bonding information given in Table 1. The structural parameters of our relaxed structures of α-Sb, β-Sb, and α-InI are in very good agreement with the theoretical data obtained by Akturk *et al.*[38] and Wang *et al.*[26] From Table 1, the α and c phases are structurally similar, and the difference between the two phases is that the cubic phase has larger isotropic in-plane lattice parameters and in-plane bond lengths than the α phase. Besides, the in-plane structural parameters (lattice constants a and b, bond-lengths d_1 and d_2) for both α and c phases become more isotropic with the increasing difference of electronegativity (Table 2) between constituents in antimonene and its isoelectronic materials from Sb to SnTe to InI. The reduced anisotropy (of structure and also of electronic properties) in the isoelectronic systems is beneficial for combining isoelectronic SnTe or InI with antimonene for a heterogeneous device, since the electronic property is nearly independent of the stacking order between the constituent materials.

Interestingly, cohesive energy $E_{\rm coh}$, which changes concomitantly with structures in the different phases, gives us some additional message. $E_{\rm coh}$ is defined as $(E_{AB} - E_A - E_B)/2$, where E_{AB} is the total energy of AB compounds per formula, E_A and E_B are the bulk energy per A and B atom, respectively. For a better comparison between the phases, $\Delta E_{\rm coh}$ $[= (E_{\rm coh} - E^{\rm c}_{\rm coh})]$ is used, with the cohesive energy of the c phase as a reference energy. $\Delta E_{\rm coh}$ as a function of structural phase for the isoelectronic materials is shown in Fig. 1(b). $\Delta E_{\rm coh}$ decreases between α and c phases, but increases between β and c phases, with the increasing ionicity in the materials from Sb to SnTe to InI, which makes β-InI very unstable, as also indicated by its phonon dispersion relation in Fig. C1 in appendix C. However, the seemingly opposite trends of $\Delta E^{\alpha,{\rm c}}_{\rm coh}$ and $\Delta E^{\beta,{\rm c}}_{\rm coh}$ can both be comprehended from the isotropy/uniformity induced by ionicity, as also illustrated in the structural change in Fig. A1 and Table 1. Long-range interaction in ionic crystals prefers uniform bonding environment[39,40] and also large bonding coordination, that is why the α phase with 5 bonding coordinations in SnTe and especially in InI is more stable energetically than the β phase with 3 bonding coordinations. Antimonene as a covalent crystal can only choose the β phase due to the covalent bond saturation, but a transition from β to α phase is possible with proper hole doping.[23] Worth pointing out that electron lone pairs in In, Sn, P, and Sb atoms play an important role in stabilizing the two-dimensional crystal of InI,[26] SnTe,[19] phosphorene,[41] and antimonene.[22] The electron lone pairs from different layers, which point outward towards the vacuum space and repel each other by Coulomb repulsion, prevent the layered InI, SnTe, and antimonene from forming 3D uniform crystal structures, which makes it possible to exfoliate from their bulk counterparts.

Table 1. Optimized lattice parameters for the nine isoelectronic family members. d_1, d_2, and d_3 are defined in Fig. C1.

	InI			SnTe			Sb		
Phase	α	β	c	α	β	c	α	β	c
a/Å	4.949	4.519	4.942	4.570	4.180	4.558	4.889	4.119	4.722
b/Å	4.943	4.519	4.934	4.549	4.180	4.553	4.353	4.119	4.363
γ/(°)	90	120	90	90	120	90	90	120	90
d_1/Å	3.498	3.119	3.498	3.169	2.947	3.231	2.639	2.892	2.950
d_2/Å	3.506	3.119	3.498	3.301	2.947	3.231	3.937	2.892	3.546
d_3/Å	3.242	–	3.241	2.929	–	2.925	2.861	–	2.867

Table 2. Electronegativity for atoms.

	In	Sn	Sb	Te	I	P
Electron affinity/eV	0.30	1.11	1.05	1.97	3.06	0.75
Electron ionization/eV	5.79	7.34	8.64	9.01	10.45	10.49
Electronegativity	1.78	1.96	2.05	2.10	2.66	2.19

The lattice dynamics is another means for determining the structural stability. In Fig. C1 in appendix C, the calculated phonon dispersion relation for the nine systems including antimonene and isoelectronic systems shows that most of the structures (i.e., α-Sb, α-InI, β-Sb, β-SnTe, c-InI) have no negative eigenfrequencies. Very few of them (α-SnTe, c-SnTe, c-Sb) have slightly negative frequencies, but in the vicinity of the Brillouin zone center. It is to note that the phonon dispersion relation given here is calculated at 0 K. We also notice that a relatively strong anharmonicity at nonzero temperature found in similar SnSe systems can stabilize the structure.[42–44] So we expect that the modes with slightly negative frequencies near the Γ point in our systems can be stabilized as well at room temperature for real applications. However, among the nine structures, hexagonal β-InI is obvi-

ously unstable, judged not only from a relatively large value of $\Delta E_{\rm coh}^{\beta,{\rm c}}$ in Fig. 1(b), but also from the negative values of phonon frequency widely distributed in BZ, indicating that this system should not exist thermodynamically.

Lattice mismatch is important to consider for isoelectronic alloying or heterostructure patterning between different systems. From Table 1, the mismatch between the three systems in the same phase is 1.2%–7.7% (α), 1.5%–8.9% (β), and 3.4%–7.8% (c). Such values may induce interlayer Moiré potential for van der Waals heterostructures,[45,46] which will bring about some extra complexity to the band structure calculations and can be considered for future study. But here, since we focus mainly on the band structure of each constituent, and especially the relative band alignment when forming vdW or alloying heterostructures, we choose to neglect the possible interlayer Moiré effect for the moment. Nevertheless, it is still challenging to take care of the lattice mismatch. Using small unit cell leads to lattice stress which influences electronic properties, while big supercell which releases stress leads to complexity of analysis due to zone folding of Brillouine zone. From the mismatch analysis, we are able to select antimonene and one isoelectronic system with the smallest lattice mismatch to have a comparision of electronic properties between band alignment schematics and real system calculation, as discussed later in Fig. 4. A very good agreement is reached, which substantiates our schematic analysis made in Fig. 3 in Subsection 3.2.

3.2. Electronic properties

The electronic band structure calculated at the HSE06 level for the three structural phases is shown in Fig. 2. From Fig. 2(a), the materials concerned here are semiconducting and all the phases except for the β phase have direct band gaps with both the conduction band minimum (CBM) and valence band maximum (VBM) located at one k point between high-symmetry Γ and Y points. The indirect band gap of the β phase has the VBM and CBM located at k points between Γ and M points. From row to row in Fig. 2(a), the band gap decreases significantly from β to α (or to c) phase, mainly due to the largely increasing VBM values from the buckled to puckered (or to cubic) geometry, as indicated later in the band alignments in Fig. 3(a).

From column to column in Fig. 2(a), independent of the structural phases, the band gap increases with increasing electronegativity difference in materials from Sb via SnTe to InI. This trend can be seen more clearly in Fig. 2(b), in which the electronegativity difference is mapped to the charge transferred between A and B in AB materials. To note that the normalized charge transferred is used here as the horizontal axis. For example, to form a totally ionized bond, one electron would be expected to transfer between In and I atoms in InI, while for SnTe two electrons would be transferred between Sn and Te atoms. However, this is not always the case, because of the electronegativity difference between the A and B atoms. In this regard, the normalized charge transferred is defined as the Bader charge divided by the number of transferred electrons needed for forming a perfect ionic bond. From Fig. 2(b), we can see an almost linear dependence of the band gap on the normalized charge transferred between constituent elements for all the materials and phases concerned. This interesting trend can be understood as follow. There is a competition between ionic bonding and covalent bonding in the materials studied here. The more normalized charge transferred between constituent elements, the more weight an ionic bonding will take, which can give rise to more localized valence electrons and then a bigger band gap.

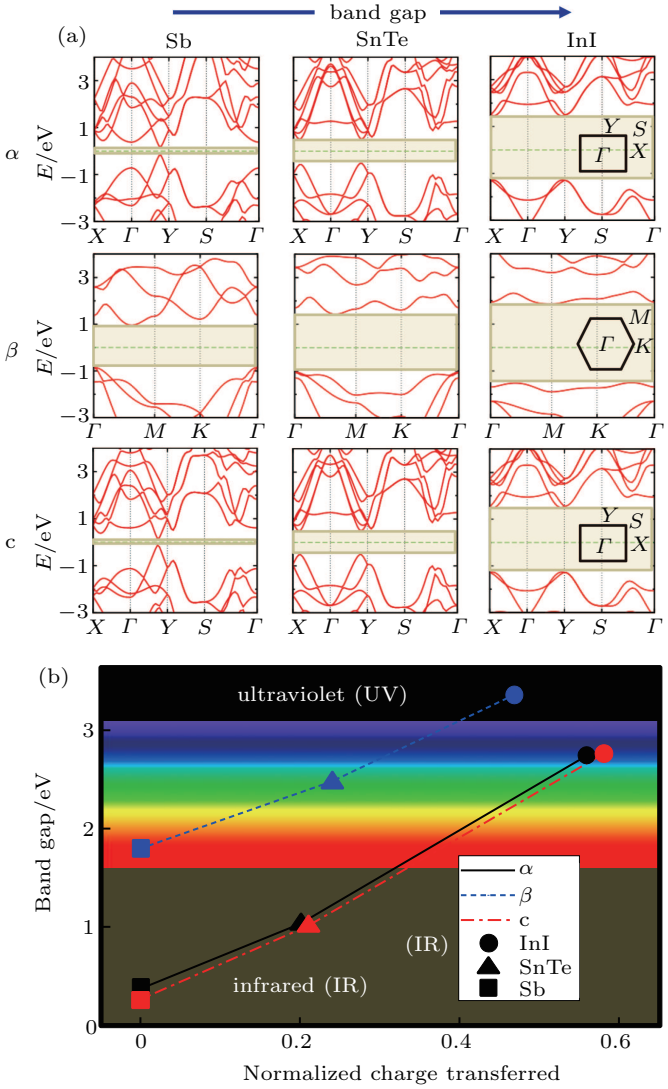

Fig. 2. (a) Electronic properties of Sb, SnTe, and InI (in column) in three phases α, β, and c (in row). Band gaps are filled with brown shadows. The arrow on the top shows the increasing band gap trend from Sb through SnTe to InI. The Brillouin zone with high-symmetry points for each phase is given in the third row. (b) The band gap within light absorbtion energy spectrum as a function of charge transfer between the constituents in each material. α, β, and c phases are shown in black solid, blue short dash, and red dash dot lines, respectively. Sb, SnTe, and InI are represented by filled square, triangle, and circle, respectively.

In Fig. 2(b), an optical spectrum from infrared (IR) to ultraviolet (UV) as background is used with the spectrum energy corresponding to band gaps, indicating that antimonene and its isoelectronic counterparts can be potential candidates for photoelectronic devices in the whole visible light region. To continually tuning the band gap in the visible light range, band alignment by vertical vdW stacking method or lateral alloying method, which mixes different phases of *AB* compounds together, can be considered.

To evaluate the carrier mobility, the effective mass of carriers at VBM/CBM is a very important parameter. From the band dispersion and curvature of VBM/CBM in Fig. 2(a), the effective mass varies slightly from Sb monolayer to its isoelectronic counterparts, but more abruptly from phase to phase. For instance, the band dispersion in the vicinity of VBM/CBM of the β phase is rather flat compared to that of the α or c phase, leading to a higher carrier effective mass in β-phase than in the other two phases. From the equvi-energy contour line of VBM/CBM plot, the carrier effective mass in Sb monolayer and the isoelectronic counterpart, even in the form of α-phase, is quite isotropic in startle contrast to black phosphorene[47] and advantageous for electronic applications independent of the crystal orientation. Also worth pointing out that the partial charge densities (frontier states) associated with VBM and CBM are vastly different in the isoelectronic counterparts of Sb, as shown in Fig. B1. The frontier states of VBMs in SnTe and InI are due to tellurium and iodine, respectively, while the frontier state of CBMs are from tin and indium. Such a spatial charge separation between VBM and CBM is also important for photo-electronic applications.

3.3. Band alignment of vertical and alloying heterostructures

For isoelectronic systems, another potential application is heterostructures, including lateral and vertical heterostructures. For heterostructures consisted of two semiconductors, band alignment is very essential, which means the band offset of the VBM and CBM between two different constituent materials *A* and *B*. Type I band alignment, with $\mathrm{VBM}_A < \mathrm{VBM}_B < \mathrm{CBM}_B < \mathrm{CBM}_A$, can be used in optical devices including light-emitting diodes and lasers;[48–50] type II heterstructures, with $\mathrm{VBM}_A < \mathrm{VBM}_B < \mathrm{CBM}_A < \mathrm{CBM}_B$, can be explored as a platform for controlling long-lived interlayer excitons,[51–53] and type III, with $\mathrm{VBM}_A < \mathrm{CBM}_A < \mathrm{VBM}_B < \mathrm{CBM}_B$, is advantageous for tunneling field effect transistor applications.[54,55] In Fig. 3(a), we show the positions of VBM and CBM relative to vacuum energy level ($E_{\mathrm{vac}} = 0$) for the nine materials. Our vertical heterostructure systems can cover all three types of band alignments. For example, type I can be found between α-InI and α-Sb; type II can be searched for between β-SnTe and β-Sb, and type III should only be found by combining Sb with the isoelectronic systems. The differentiation of three types of band alignments is more directly shown in the periodic table of heterstructures in Fig. 3(b). Except for nine homogeneous bilayers and also heterstructures due to unstable β-InI, there are 28 potential vdW heterostructures from the upper half of the table, in which there are 11 type I (in cyan), 11 type II (in purple), and 6 type III (in pink). Among them, Sb takes a leading role in forming all the three types of band alignments with its isoelectronic systems, for example, type-I (6/11), type-II (6/11), and type-III (6/6), mainly due to its high VBM and narrow band gap in antimonene.

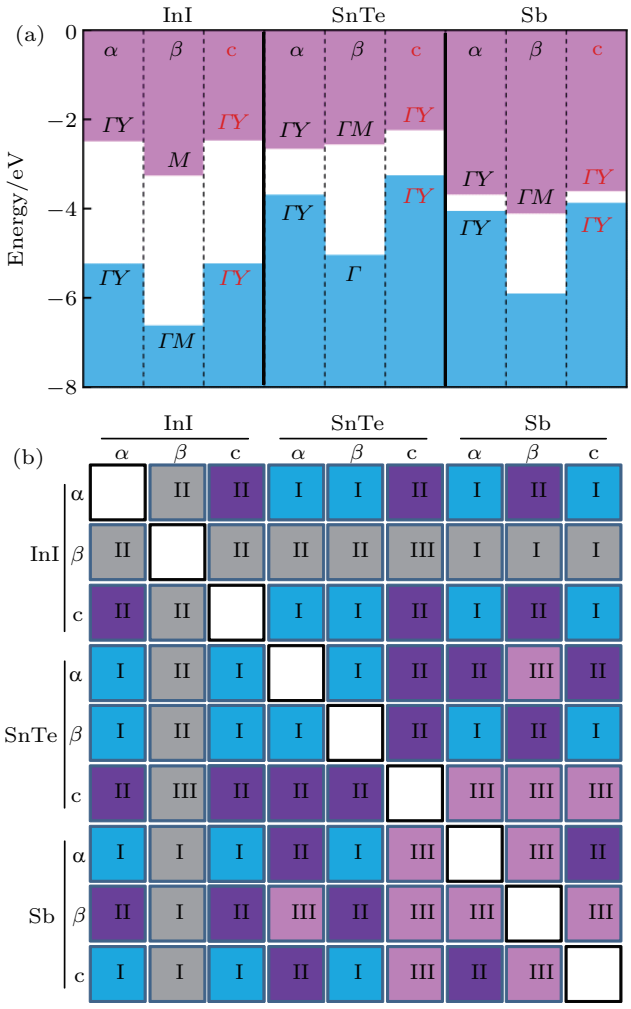

Fig. 3. (a) Band alignment for InI, SnTe, and Sb in α, β, and c phases. The most stable phase is marked in red color. Note that the vacuum energies are set to zero when obtaining the band diagrams. (b) Periodic table of heterostructures. Types I, II, and III are represented by cyan, purple, and pink boxes, respectively. The spots related to the unstable β-InI is marked in grey box.

The results presented in Fig. 3 should supply a useful guidance for experimentalists for designing selective heterstructures. To substantiate the validity of the band alignment analysis above, as an example, we calculate the electronic band structure of type-II β-SnTe/β-Sb vertical vdW heterostructure with AB (Bernal) stacking, as well as of type-II α-SnTe/α-Sb lateral alloying heterostructure, as shown in

Figs. 4(a) and 4(b). In Fig. 4(a), the combined band diagram in the middle maintains the band structure features of constituents in the vicinity of the band gap. The CBM is mainly contributed by that of β-Sb, while the VBM from that of β-SnTe, well reproducing the schematic band alignment analysis even in a quantitative manner. Likewise, in Fig. 4(b), alloying α-SnTe with α-Sb with Sb randomly distributed in the crystal can still preserve the main band structure characteristic, validating once more the schematic band alignment analysis even in a more complicated alloying case.

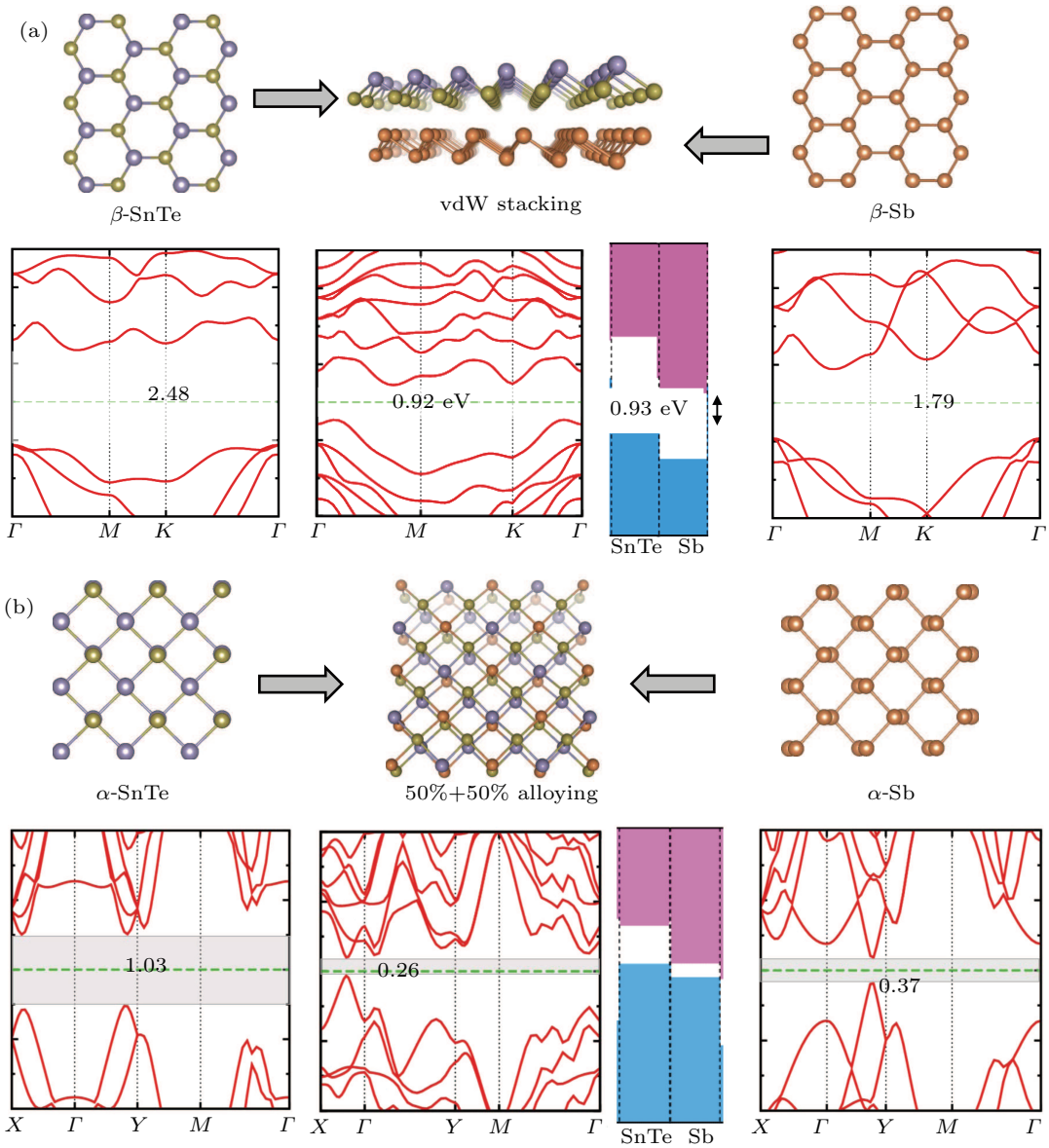

Fig. 4. Electronic properties of (a) vertical vdW and (b) alloying SnTe/Sb heterstructures. (a) For β-SnTe/β-Sb vertical vdW heterstructure. The band gap size, CBM and VBM positions from both schematic band alignment analysis and calculation agree well. (b) For α-SnTe/α-Sb alloying (50% each), schematic band alignment analysis also agrees well with alloying band structure calculation.

To show the enhancement of the heterostructure upon constituent monolayers for optoelectronic application, we show in Fig. D1 the calculated absorption data for the three systems, the β-Sb/β-SnTe heterostructure, β-Sb monolayer, and β-SnTe monolayer in black, blue, and red, respectively. From monolayers to heterostructure, the optical spectra have some significant changes as follows. (i) Peak absorption occurs below the band gaps of the two monolayers, indicating that a type-II band alignment is achieved and the interlayer electronic transition appears between β-Sb and β-SnTe sublayers. We do extend the optoelectronic applications towards low-frequency region (such as infrared, and far infrared). (ii) The optical absorption intensity changes abruptly. The intensity of type-II heterostructure is larger than the sum of two single monolayers, indicating that besides the optical-induced intra-layer electronic transition in each sublayer, there is an additional inter-layer electronic transition, giving rise to some long lifetime interlayer exciton, which is very advantageous for optoelectronic applications over the monolayers.

4. Conclusion

Using *ab initio* density functional theory calculations, we explore three stable structural phases, namely, α, β, and c, of two-dimensional antimonene, as well as its isoelectronic counterparts SnTe and InI. We find that their band gap increases monotonically from Sb to SnTe to InI along with an increase in ionicity, independent of the structural phase. The band gaps of this family of materials cover the entire visible-light energy spectrum, ranging from 0.26 eV to 3.365 eV, for optoelectronic applications. Meanwhile, we explore band-edge positions of these materials and demonstrate that all three types of band alignments can be achieved by combining antimonene with its isoelectronic counterpart to form heterostructures. The richness in electronic properties for this family of isoelectronic materials sheds light on possibilities to tailor the fundamental band gap of antimonene via alloying or forming vertical heterostructures.

Appendix A: Relaxed atomic structures and lattice parameters of Sb and its isoelectronic materials

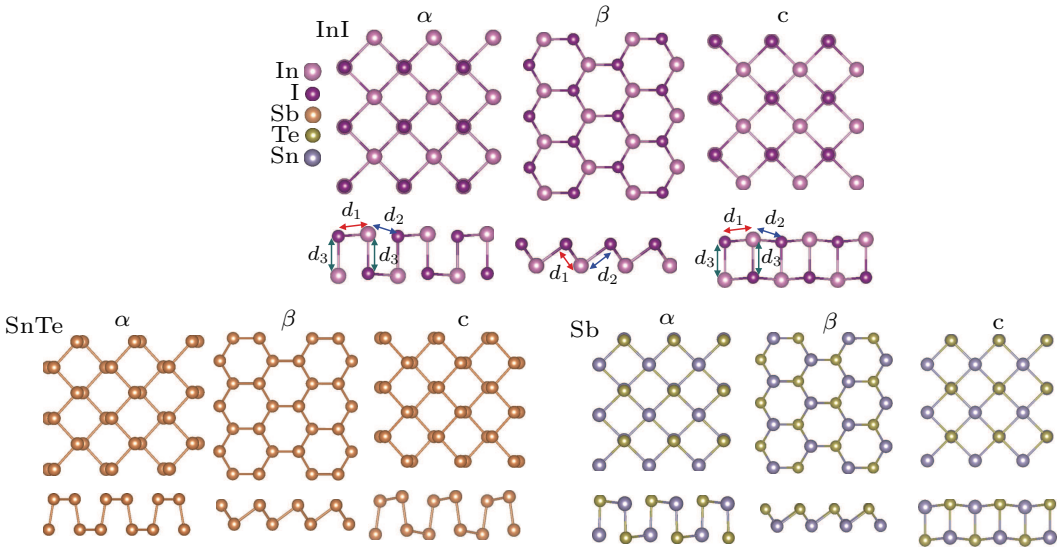

Fig. A1. Optimized atomic structure of InI, SnTe, and Sb (from top to bottom) in three phases α, β, and c (from left to right).

Appendix B: Partial charge densities

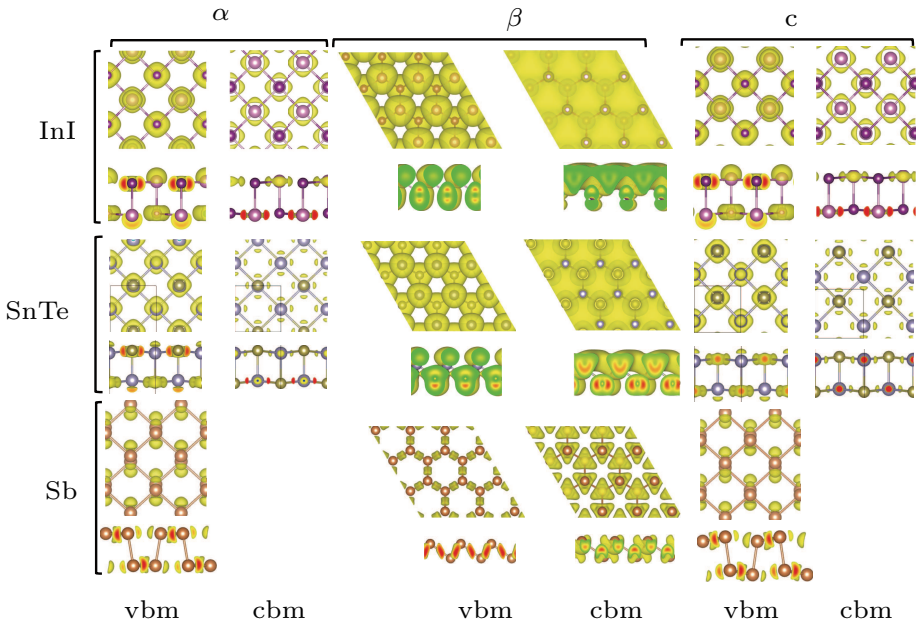

Fig. B1. Partial charge densities near VBM and CBM for InI, SnTe, and Sb (from top to bottom) in three phases α, β and c (from left to right). For both α and c phases of Sb, the partial charge densities are calculated in the range of $E_F \pm 0.1$ eV.

Appendix C: Phonon dispersion relation

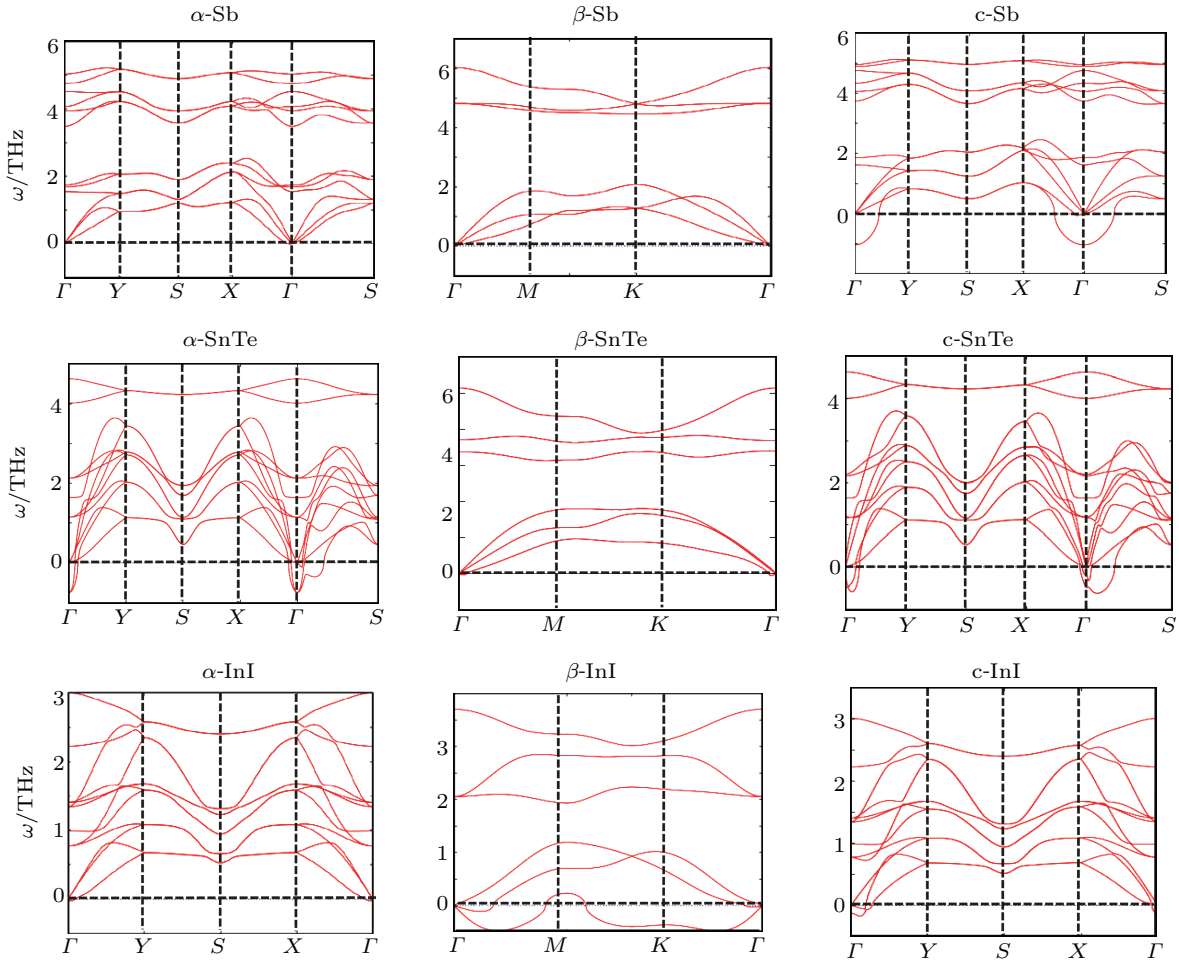

Fig. C1. Phonon dispersion relation for InI, SnTe, and Sb (from top to bottom) in three phases α, β and c (from left to right).

Appendix D: Optical absorption

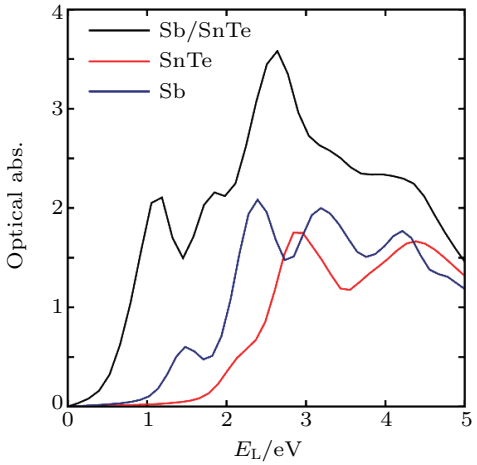

Fig. D1. Optical absorption of β-Sb/β-SnTe heterostructure (black), β-Sb monolayer (blue), β-SnTe monolayer (red).

References

[1] Novoselov K S, Geim A K, Morozov S V, Jiang D, Zhang Y, Dubonos S V, Grigorieva I V and Firsov A A 2004 *Science* **306** 666

[2] Radisavljevic B, Radenovic A, Brivio J, Giacometti V and Kis A 2011 *Nature Nanotech* **6** 147

[3] Guo H H, Yang, T, Yamamoto M, Zhou L, Ishikawa R, Ueno K, Tsukagoshi K, Zhang Z D, Dresselhaus M S and Saito R 2015 *Phys. Rev. B* **91** 205415

[4] Tao P, Guo H H, Yang T and Zhang Z D 2014 *J. Appl. Phys.* **115** 054305

[5] Guo H H, Yang T, Tao P, Wang Y and Zhang Z D 2013 *J. Appl. Phys.* **113** 013709

[6] Guo H H, Yang T, Tao P and Zhang Z D 2014 *Chin. Phys. B* **23** 017201

[7] Huang S X, Tatsumi Y, Ling X, *et al.* 2016 *ACS Nano* **10** 8964

[8] Wang Z, Zhang T Y, Ding M, *et al.* 2018 *Nat. Nanotechnol.* **13** 554

[9] Wang H, Chen M L, Zhu M J, *et al.* 2019 *Nature Commun.* **10** 2302

[10] Liu H, Neal A T, Zhu Z, Luo Z, Xu X, Tománek D and Ye P D 2014 *ACS Nano* **8** 4033

[11] Li L, Yu Y, Ye G J, Ge Q, Ou X, Wu H, Feng D, Chen X H and Zhang Y 2014 *Nat. Nanotech.* **9** 372

[12] Ling X, Wang H, Huang S, Xia F and Dresselhaus M S 2015 *Proc. Natl. Acad. Sci. USA* **112** 4523

[13] Yang T, Dong B, Wang J, Zhang Z, Guan J, Kuntz K, Warren S C and Tománek D 2015 *Phys. Rev. B* **92** 125412

[14] Kuntz K L, Wells R A, Hu J, Yang T, Dong B J, Guo H H, Woomer A H, Druffel D L, Alabanza A, Tománek D and Warren S C 2017 *ACS Appl. Mater. & Inter.* **9** 9126

[15] Sharma S, Kumar S and Schwingenschlgl U 2017 *Phys. Rev. Appl.* **8** 4

[16] Zhu Z, Guan J and Tománek D 2015 *Nano Lett.* **15** 6042

[17] Zhu Z, Guan J, Liu D and Tománek D 2015 *ACS Nano* **9** 8284

[18] Zhu Z, Dong B J, Guo H H, Yang T and Zhang Z D 2020 *Chin. Phys. B* **29** 046101

[19] Dong B J, Wang Z H, Hung N T, Oganov A R, Yang T, Saito R and Zhang Z D 2019 *Phys. Rev. Materials* **3** 013405

[20] Novoselov K S, Mishchenko A, Carvalho, A and Castro Neto A H 2016 *Science* **353** aac9439
[21] Zhu Z, Guan J and Tomanek D 2015 *Phys. Rev. B* **91** 161404(R)
[22] Zhang S, Yan Z, Li Y, Chen Z and Zeng H 2015 *Angewandte Chemie* **127** 3155
[23] Wang J, Yang T, Zhang Z and Yang L 2018 *Appl. Phys. Lett.* **112** 213104
[24] Singh D, Gupta S K, Sonvanea Y and Lukaćević I 2016 *J. Mater. Chem. C* **4** 6386
[25] Guan J, Zhu Z and Tomanek D 2014 *ACS Nano* **8** 12763
[26] Wang J, Dong B J, Guo H, Yang T, Zhu Z, Hu G, Saito R and Zhang Z D 2017 *Phys. Rev. B* **95** 045404
[27] Kresse G and Furthmuller J 1996 *Phys. Rev. B* **54** 11169
[28] Kresse G and Joubert D 1999 *Phys. Rev. B* **59** 1758
[29] Perdew J P, Burke K and Ernzerhof M 1996 *Phys. Rev. Lett.* **77** 3865
[30] Ozcelik V O, Azadani J G, Yang C, Koester S J and Low T 2016 *Phys. Rev. B* **94** 035125
[31] Monkhorst H J and Pack J D 1976 *Phys. Rev. B* **13** 5188
[32] Hestenes M R and Stiefel E 1952 *J. Res. Natl. Bur. Stand.* **49** 409
[33] Klimeš J, Bowler D R and Michaelides A 2011 *Phys. Rev. B* **83** 195131
[34] Togo A and Tanaka I 2015 *Scripta Materialia* **108** 1
[35] Baroni S, de Gironcoli S and Dal Corso A 2001 *Rev. Mod. Phys.* **73** 515
[36] Gajdoš M, Hummer K, Kresse G, Furthmüller J and Bechstedt F 2006 *Phys. Rev. B* **73** 045112
[37] Zimmermann H 2000 *Integrated Silicon Optoelectronics, Springer Series in Optical Sciences* (New York: Springer)
[38] Aktuřk O Ü, Ožcelik V O and Ciraci S 2015 *Phys. Rev. B* **91** 235446
[39] Harrison W A 1989 *Electronic Structure and the Properties of Solids: The Physics of the Chemical Bond* (New York: Dover Publications)
[40] Harrison W A 1999 *Elementary electronic structure* (Sigapore: World Scientific)
[41] Zhu Z and Tománek D 2014 *Phys. Rev. Lett.* **112** 176802
[42] Aseginolaza U, Bianco R, Monacelli L, Paulatto L, Calandra M, Mauri F, Bergara A and Errea I 2019 *Phys. Rev. Lett.* **122** 075901
[43] Aseginolaza U, Bianco R, Monacelli L, Paulatto L, Calandra M, Mauri F, Bergara A and Errea I 2019 *Phys. Rev. B* **100** 214307
[44] Errea I, Rousseau B and Bergara A 2011 *Phys. Rev. Lett.* **106** 165501
[45] Wallbank J R, Mucha-Kruczyński M, Chen X and Fal'ko V I 2015 *Ann. Phys.* **527** 359
[46] Carr S, Massatt D, Torrisi S B, Cazeaux P, Luskin M and Kaxiras E 2018 *Phys. Rev. B* **98** 224102
[47] Rodin A S, Carvalho A and Castro Neto A H 2014 *Phys. Rev. Lett.* **112** 176801
[48] Nakamura S, Senoh M, Iwasa N and Nagahama S 1995 *Jpn. J. Appl. Phys.* **34** L797
[49] Withers F, Pozo-Zamudio O D, Mishchenko A, *et al.* 2015 *Nat. Mater.* **14** 301
[50] Politano A, Slotman G J, Roldán R, Chiarello G, Camp D, Katsnelson M I and Yuan S J 2017 *2D Mater.* **4** 021001
[51] Calman E, Dorow C, Fogler M, Butov L, Hu S, Mishchenko A and Geim A 2016 *Appl. Phys. Lett.* **108** 101901
[52] Jauregui L A, Joe, A Y, Pistunova K, *et al.* 2019 *Science* **366** 870
[53] Shim J, Kang D H, Kim Y, Kum H, Kong W, Bae S H, Almansouri I, Lee K, Park J H and Kim J 2018 *Carbon* **133** 78
[54] Koswatta S O, Koester S J and Haensch W 2010 *IEEE Trans. Electron Devices* **57** 3222
[55] Li X X, Fan Z, Liu P, *et al.* 2017 *Nat. Commun.* **8** 970